ACS Catalysis

Research Article

pubs.acs.org/acscatalysis

Natural Alginate as a Graphene Precursor and Template in the Synthesis of Nanoparticulate Ceria/Graphene Water Oxidation Photocatalysts

Cristina Lavorato,[†] Ana Primo,[‡] Raffaele Molinari,[†] and Hermenegildo García*[,‡]

[†]Department of Environmental and Chemical Engineering, University of Calabria, Via P. Bucci 44A, 87036 Rende, CS, Italy

[‡]Instituto Universitario de Tecnología Química, Universitat Politècnica de València, Av. de los Naranjos s/n, 46022 Valencia, Spain

Supporting Information

ABSTRACT: Using alginate, a natural polysaccharide from algae, simultaneously as a graphene precursor and a templating agent for ceria nanoparticles, we have prepared a series of materials consisting of highly crystalline ceria nanoparticles embedded on a few-layer graphene matrix. XPS analysis indicates that the predominant oxidation state of Ce in the as-synthesized CeO_x/graphene material is +III (over 80 atom %). Varying the weight percentage of ceria/alginate and the pyrolysis temperature enabled the preparation of a ceria/graphene photocatalyst that exhibits about 3 times higher photocatalytic activity for water oxidation to oxygen than commercial ceria. Our results on the ceria/graphene composite as a photocatalyst for water oxidation expand and complement the well-known effect of graphene to increase the photocatalytic efficiency of titania/graphene composites.

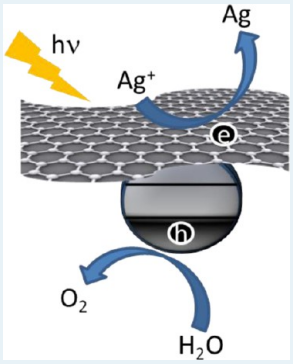

KEYWORDS: *photocatalysis, graphene, biomass, alginate, water splitting*

1. INTRODUCTION

Semiconducting metal oxides, such as TiO_2, ZnO, and WO_3, exhibit photocatalytic activity whose efficiency depends on many factors related to their synthesis and textural properties.[1,2] In particular, the morphology and the average size of the particles are key parameters that exert a strong influence on the photocatalytic performance of the materials.[3,4] Besides the particle size, the surface functionality and hydrophobicity as well as the density of surface hydroxyl groups also play important roles in the photocatalytic activity. Surface area, particle size, and density of hydroxyl groups are largely determined by the synthetic methodology used for the preparation of the material.[5,6] In this context, we[7,8] and others[9,10] have recently reported the use of biopolymers as templating agents for the synthesis of TiO_2 and CeO_2 nanoparticles (NPs) having a high photocatalytic activity for water splitting, either for reduction (TiO_2) or for oxidation (CeO_2). In materials science, the use of templates for the synthesis of solids is a general methodology to gain control of the morphology and structure of the particles, and the use of natural biopolymers as templates is an illustrative example of biomass waste valorization. Continuing with the application of natural biopolymers as templates for the synthesis of photocatalysts having activity for water splitting, herein we show an original process that leads simultaneously to the generation of metal oxide NPs acting as a photocatalyst as well as graphene (G) acting as a promoter in contact with ceria NPs to improve their efficiency.

In the case of TiO_2,[11,12] it has been well-documented that intimate contact with G sheets can increase by a factor of 2 the photocatalytic activity inherent to TiO_2,[13] a fact that has been attributed to more efficient charge separation originating from the migration of electrons from the TiO_2 conduction band to G (Scheme 1). It has been found that analogous processes can also operate for other semiconductors, including ZnO, WO_3, and Fe_2O_3, and similarly to TiO_2, the photocatalytic activity of these semiconductors is also enhanced to various extents by adequate interfacial contact with G-based carbons.[14−19] Recently it has been found that ceria NPs well-dispersed in reconstituted G oxide are more efficient as a photocatalyst than the same ceria sample alone for the degradation of methylene blue upon irradiation with simulated sunlight, confirming the validity of this concept also for ceria.[20] In the present article, we provide an additional example involving the preparation of highly crystalline ceria NPs embedded in a graphene matrix formed by pyrolysis under anaerobic conditions of the polymeric template employed in the synthesis and the use of this composite as a photocatalyst for water oxidation. Although the use of ceria as a photocatalyst is much less documented than the use of TiO_2, it has been found that ceria is highly active for photocatalytic oxygen generation from water in the presence of sacrificial electron acceptors.[7] Photocatalytic water oxidation is a challenging process since it is mechanistically

Received: July 18, 2013
Revised: December 28, 2013
Published: December 30, 2013

Scheme 1. Mechanism Proposed for the Enhanced Charge Separation in Semiconductor−G Composites: (i) Light Absorption Leading to Charge Separation with the Creation of Electrons and Holes; (ii) Electron Migration from the Semiconductor Conduction Band to G

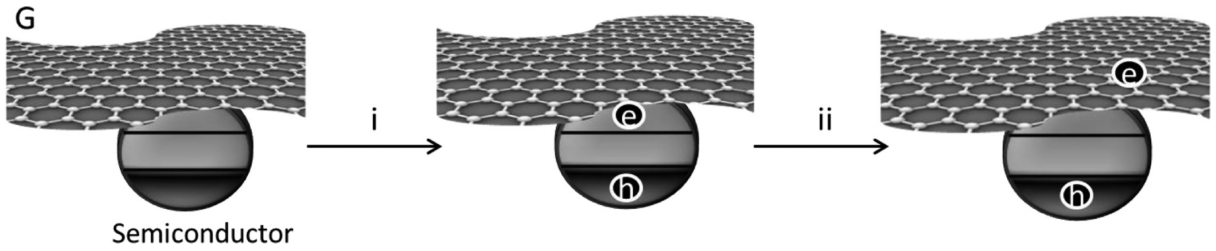

complex requiring the removal of four electrons and protons from water. This type of composite based on G-supported ceria has been used as electrodes for the electrochemical oxidation of hydrazine.[21] In addition, samples of graphene-coated ceria containing well-dispersed Ag NPs have also been used as catalysts for the reduction of *p*-nitrophenol by $NaBH_4$ as a model reaction.[22] The results described below show the potential use of natural abundant biopolymers considered as biomass waste for the preparation of photocatalysts with enhanced performance with respect to the conventional hydrothermal synthesis of these metal oxides and represent a clear example of biomass valorization.

2. EXPERIMENTAL SECTION

2.1. Photocatalytic Oxygen Production Tests. Irradiations were carried out for 4 h using the output of a 200 W xenon-doped mercury lamp without a cutoff filter (Hamamatsu Lightningcure LC8) emitting UV light. The distance between the light source and the top of the reactor was 0.5 cm. The photoreactor was a cylindrical Pyrex vessel (48 mL total volume) with an inlet and outlet having a manometer and a thermocouple to determine the pressure and the temperature in the gas phase, respectively. All of the experimental tests were conducted at room temperature, and the temperature of the gas phase for all of the experimental tests was in the range 25−30 °C. To ensure the absence of oxygen, the system was purged with an argon flow for 30 min before irradiation. The photocatalytic solution (25 mL) containing water, 0.01 M $AgNO_3$ as a sacrificial electron acceptor, and 20 mg of photocatalyst was continuously stirred magnetically during irradiation. The amount of oxygen evolved in the photoreactor during the irradiation was quantified using a gas chromatograph (GS-MOL 15 m × 0.55 mm i.d. column and TCD from J&W Scientific) previously calibrated with standards, and the amount of oxygen generated was calculated taking into account the ideal gas law ($n = PV/RT$).

2.2. Synthesis of CeO_x/Graphene. All of the reagents used were from commercial suppliers and of analytical grade. CeO_2/graphene samples were synthesized starting from an aqueous solution of commercial alginic acid sodium salt (Aldrich, 10 g L^{-1}) prepared by dissolving 1 g of sodium alginate in 100 mL by magnetic stirring for 2−3 h. Then the solution was filtered to remove insoluble impurities. Next, the clear solution was precipitated in the shape of millimetric spheres by adding dropwise one of two different aqueous solutions of $(NH_4)_2Ce(NO_3)_6$ (55 or 110 g L^{-1}). After 12 h, the spherical beads containing Ce^{4+} were collected by filtration, washed with water, and then converted into alcogels by gradual replacement of water by ethanol. This replacement was carried out by stirring the spherical beads in 50 mL of solutions with increasing alcohol concentration. Five solutions containing 10, 20, 40, 80, and 100 vol % ethanol were consecutively used. Subsequently, the resulting alcogel beads were submitted to supercritical CO_2 drying (above 73 bar and 31 °C) using an E3000 critical point drying apparatus to yield aerogel beads. These aerogel beads were pyrolyzed in an oven under argon by heating initially at 200 °C for 2 h for annealing and subsequently at a 10 °C min^{-1} temperature ramp up to either 800 or 900 °C, depending on the sample, for calcination. The final temperature was maintained for 2 h. Subsequently, the resulting residue was allowed to cool at ambient temperature. Finally, CeO_x/graphene sheet (CeO_x/G) samples were obtained by grinding the graphitic beads and then dispersing the particles into an aqueous solution that was ultrasonicated for at least 1 h before the photocatalytic tests. Commercial CeO_2 from Aldrich (ref. no. 544841-5G, <25 nm average size) was used for comparison.

2.3. Measurements of Textural and Analytical Properties. Raman spectra were recorded at ambient temperature with 514 nm laser excitation at 2 mW power using a Renishaw In Via Raman spectrometer equipped with a CCD detector. Transmission electron microscopy (TEM) images were recorded in a Philips CM300 FEG system with an operating voltage of 100 kV. The solid samples (1−3 mg) were suspended in water (3 mL) and submitted to sonication (300 W) for at least 30 min, after which a microdrop was dropped on a lacey carbon-coated Cu grid. X-ray photoelectron spectroscopy (XPS) was performed on a SPECS spectrometer equipped with a Phoibos 150 9MCD detector using a non-monochromatic X-ray source (Al and Mg) operating at 200 W. The samples were evacuated in the prechamber of the spectrometer at 1 × 10^{-9} mbar. The samples were activated in situ in a nitrogen flow at 450 °C for 3 h followed by evacuation at 10^{-8} mbar. Deconvolution and fitting of the experimental peaks was carried out after nonlinear Shirley-type background subtraction and peak correction by the transmission function of the spectrometer. Atomic force microscopy (AFM) measurements were conducted using contact mode in air at ambient temperature using a Veeco AFM apparatus. To ensure the absence of oxygen, the entire system was purged with an argon flow for 30 min before irradiation.

3. RESULTS AND DISCUSSION

3.1. Synthesis and Characterization of CeO_x/G Composites. In the present study, we prepared a series of CeO_x NPs embedded on a G-based matrix. The two parameters that were optimized during the synthesis were the temperature of the pyrolysis process (either 800 or 900 °C) and the weight percentage of the biopolymer in the material. The synthesis of the photocatalysts is summarized in Scheme 2. The process

dx.doi.org/10.1021/cs401068m | ACS Catal. 2014, 4, 497−504

Scheme 2. Procedure for the Synthesis of CeO_x/G Samples: (i) Precipitation of the Ce^{3+}-Containing Alginate Hydrogel with $(NH_4)_2Ce(NO_3)_6$; (ii) Drying by H_2O to EtOH Exchange and Supercritical CO_2 Drying; (iii) Pyrolysis under Ar Flow

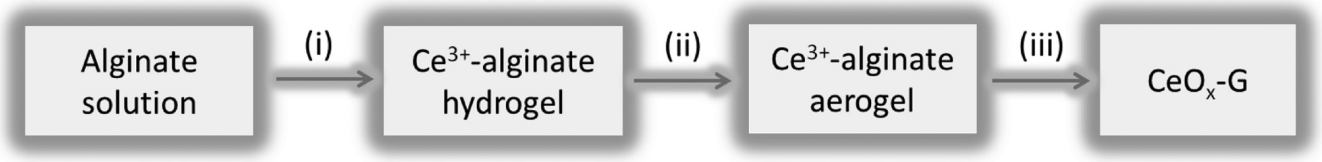

started with the precipitation of cerium alginate beads by dropping an aqueous alginate solution into an aqueous solution of cerium ammonium nitrate [step (i) in Scheme 2]. It is well-known in the literature that alginate forms solid precipitates with Ca^{2+} as well as other di- and tripositive metal cations.[23,24] The hydrated cerium alginate beads were dried by gradual exchange of water with ethanol by stirring the cerium alginate beads consecutively in a series of five water/ethanol solutions of increasing percentage of ethanol from 20 to 100 vol %. Finally the resulting alcogel beads were submitted to supercritical CO_2 drying to form aerogels having large surface areas of up to 400 m^2/g [step (ii) in Scheme 2].[7] Previously, calcination of these cerium alginate aerogel beads in air to produce the combustion of the natural alginate polymer was reported.[7] In that case, aerobic combustion led to the complete removal of the organic material, leaving CeO_2 particles. In the present case, in contrast, the cerium alginate beads were submitted to pyrolysis under an inert atmosphere at temperatures in the range from 800 to 900 °C [step (iii) in Scheme 2]. This thermal treatment led on one hand to the formation of CeO_x NPs, while on the other hand the oligosaccharide was decomposed to form graphitic carbons. In the literature it has been reported that pyrolysis of alginate beads without Ce^{3+} ions leads to the formation of graphitic carbon residues.[25] In the present case, the process undergone by alginate was similar to the one reported leading to graphitic residues, except that the sample also contained $Ce^{4+/3+}$ that evolved to nonstoichiometric CeO_x. Ce^{3+} ions should be formed by water and carbochemical reduction of Ce^{4+} to Ce^{3+} accompanied by the oxidation of carbon to CO_2 under the pyrolysis conditions (see below for the XPS characterization). In that way, this CeO_x/G composite in which the two components are in contact can have interesting photocatalytic properties derived from the combination of cerium oxide embedded in G-based carbon.

The resulting four CeO_x/G materials were characterized by analytical, textural, and spectroscopic techniques. Combustion chemical analysis showed that the samples contain different percentages of carbon related to the composition of the initial solution and to the pyrolysis temperature (Table 1).

TEM images of the materials show the presence of highly crystalline CeO_x NPs embedded inside the carbon matrix (Figure 1). It was observed that the CeO_x NPs presented well-defined triangular, cubic, or hexagonal shapes with a narrow particle size distribution that depended on the calcination temperature and the G content. With a Gatan imaging filter (GIF), an energy-filtered imaging technique, we mapped the elemental distributions of Ce, O, and C in a selected area of the microscopy image and found that these regular NPs correspond to CeO_x NPs that are covered by a C matrix (Figure 2). In agreement with reported TEM images of related samples obtained by alginate pyrolysis, the TEM images show that the carbon material is constituted by imperfect stacking of graphenic layers that in the inner part of the wall have a

Table 1. List of the CeO_x/G Samples Studied, Details of the Preparation Procedure, and Percentages of Graphitic Carbon Content

sample	C content (%)	CeO_x average particle size (nm)[a]	amount of $(NH_4)_2Ce(NO_3)_6$ (g/g of alginate)	pyrolysis temperature (°C)
$(CeO_x/G)_A$	2.5	28.3	11	900
$(CeO_x/G)_B$	5.19	25.3	11	800
$(CeO_x/G)_C$	0.015	117.4	22	900
$(CeO_x/G)_D$	0.56	29.1	22	800

[a]Determined by the Scherrer equation using the 111 XRD peak.

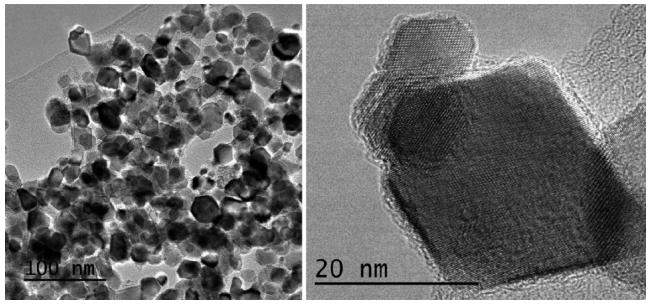

Figure 1. (left) TEM and (right) high-resolution TEM images of $(CeO_x/G)_A$. The morphology of the CeO_x crystallites with defined geometrical shapes can be clearly observed. The sample was prepared by suspending the solid in water and sonicating, after which a microdrop was deposited on a lacey carbon-coated copper grid holder.

spongelike morphology probably caused by the evolution of a large quantity of gases during the thermal treatment.[25] It has already been stated that this imperfect stacking of the graphenic layers, as also revealed by the broad X-ray diffraction (XRD) peak at $2\theta = 26°$, is suitable for performing exfoliation of the individual G layers to reach, in aqueous suspension, the state of single-layer or few-layer G.[26] On the other hand, wide-angle XRD also showed the expected peaks perfectly indexed as the face-centered cubic fluorite phase of well-crystallized CeO_x materials ($Fm\bar{3}m$, JCPDS no. 34-0394) with lattice constant $a = b = c = 5.4141$ Å (Figure 3). The average CeO_x particle size for each sample was determined from the most intense 111 peak by applying the Scherrer equation, and it was found that the average particle size increased with increasing calcination temperature and decreasing G content, from 29.1 ± 0.5 nm (calcination at 800 °C, high G content) to 117.4 ± 0.5 nm (calcination at 900 °C, low G content), as indicated in Table 1. The relatively small average particle size of CeO_x NPs in spite of the high temperatures has been observed previously for TiO_2[8] and has been attributed to the effect of the biopolymer and the materials derived from it during the thermal treatment,

dx.doi.org/10.1021/cs401068m | ACS Catal. 2014, 4, 497−504

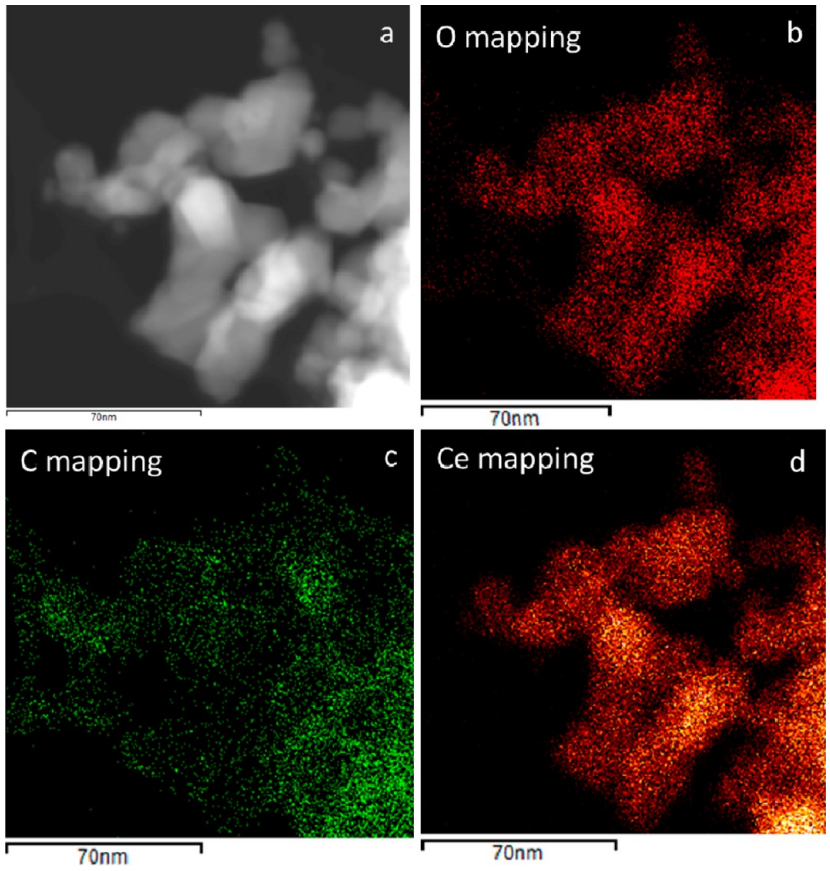

Figure 2. (a) Zero-loss TEM image of a $(CeO_x/G)_A$ sample. (b–d) GIF images showing elemental distributions of oxygen, carbon, and cerium, respectively. It should be noted that the O and Ce mapping images are coincident, while C is spread over a larger area covering the CeO_x NPs.

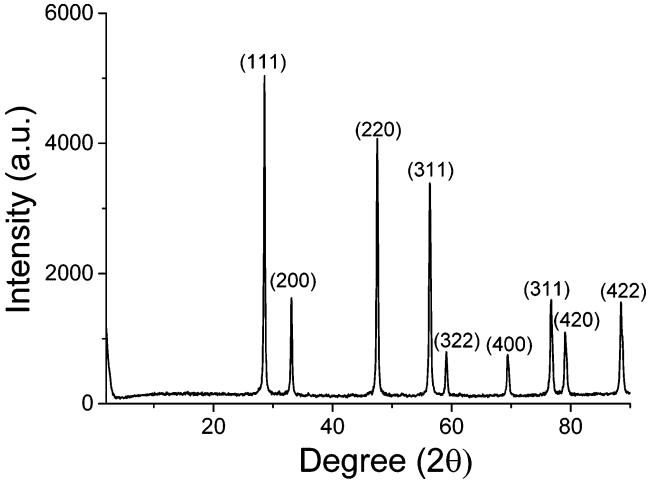

Figure 3. XRD pattern of the $(CeO_x/G)_A$ sample. The peaks have been indexed according to the literature.

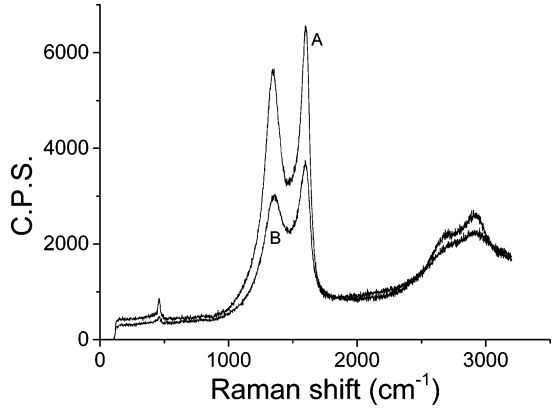

Figure 4. Raman spectra of (A) $(CeO_x/G)_A$ and (B) $(CeO_x/G)_B$ recorded using a 514 nm laser. The peak corresponding to ceria appears at 462 cm^{-1}, while the most intense peaks correspond to G.

which control the growth and agglomeration of the inorganic NPs.

Raman spectroscopy is a suitable technique to report on the nature of the carbonaceous materials[27] and CeO_x nanoparticles.[28−31] In all cases, we were able to monitor the characteristic "G" band (in-plane vibrational mode of graphenic sp^2 carbons) at 1600 cm^{-1} and "D" band (associated with defects) at 1346 cm^{-1} that correspond to the peaks of graphenic carbon with defects on the G layers (Figure 4). With regard to the CeO_x NPs, the peak at 462 cm^{-1} is related to symmetrical stretching of the $Ce-O_8$ vibrational unit, corresponding to the triply degenerate F_{2g} mode of fluorite CeO_2 and the only one allowed in first-order Raman scattering. FT-IR spectroscopy (see Figure S5 in the Supporting Information) showed the absence of bands attributable to G oxide as well as the lack of C−H, carboxylic acid, and carboxylate groups. Only bands associated with the presence of adsorbed water (broad and intense O−H strectching band at 3400 cm^{-1} and weak bending peak at 1640 cm^{-1}) and the Ce−O peak at 462 cm^{-1} were observed, as previously reported.[21] Overall, the FT-IR spectra show the transformation of initial

dx.doi.org/10.1021/cs401068m | ACS Catal. 2014, 4, 497−504

alginate (having strong IR bands) into a carbonaceous material and formation of the inorganic metal oxide.

UV−vis absorption spectra of the samples were recorded (see the Supporting Information), allowing optical estimation of the band gap from the onset of the absorption band appearing at 388 nm. Extrapolation of the linear part of the absorption band gave a band gap of 3.15 or 3.28 eV depending on the CeO_x/G sample. Slight variations in the UV−vis absorption spectra of ceria covered by reconstituted G oxide have been taken in the literature[21] to indicate strong interactions between these two components by analogy with the shifts observed for ZnO/reconstituted G oxide[32] and Bi_2O_3/reconstituted G oxide.[33]

XPS also reports on the composition of the series of samples and the oxidation states of the elements from the binding energies of these elements. In the present case, XPS of the series of CeO_x/G samples allowed detection of the C 1s peak (Figure 5). Deconvolution of the experimental peak showed

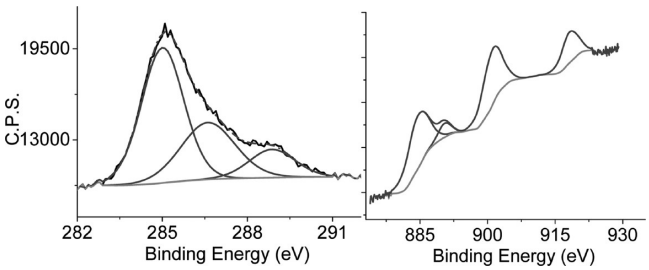

Figure 5. (a) C 1s peak and the best fit considering three major components, one corresponding to graphenic sp^2 C and the other two to C bonded to oxygen. (b) Ce 3d peaks showing the predominant presence of Ce(III) (peaks at 885.6 and 901.8 eV) vs Ce(IV) (peak at 918.6 eV) in the $(CeO_x/G)_A$ sample.

three components appearing at 285.0, 286.5, and 288.8 eV, the first one corresponding to sp^2 graphenic carbons and the second and third to carbon atoms bonded to oxygen. The relative proportions of these three peaks differed from one sample to another, indicating that the crystallinity, reflected by the relative proportion of graphenic carbons, depends on the percentage of ceria and the pyrolysis temperature. Interestingly, analysis of the 3d peak of Ce revealed a large proportion of Ce(III) with respect to Ce(IV) (Figure 5).[21] This fact is not totally unexpected considering that pyrolysis was carried out under reductive conditions required for the graphitization of alginate. In a related precedent, pyrolysis of a hybrid Ni,Mn hydrotalcite with G oxide, the reduction of Ni(II) to Ni(0) was observed,[34] and these reductive conditions should also be responsible in the present case for the predominant presence of Ce(III) over Ce(IV).

Concerning the predominant percentage of Ce(III) with respect to Ce(IV) in the CeO_x/G composites and its potential influence on the behavior as the composite as a semiconductor, it is worth commenting that CeO_2 constituted by micrometric particles is an insulator oxide and not semiconductor material.[35] By a decrease in the particle size from micrometers into the nanometric domain, it has been observed that the presence of oxygen vacancies in the lattice and the increasing confusion between the +IV and +III oxidation states are responsible for this behavior as a semiconductor.[36] Thus, in the present case, the nanometric size of CeO_x and the presence of the +III and +IV oxidation states are adequate traits for observation of the photocatalytic activity of ceria derived from the semiconducting properties. Nevertheless, the fact that the stoichiometry is far from CeO_2 in our samples is the reason why we prefer to denote our samples as CeO_x.

3.2. Comparative Activity of CeO_x/G and Commercial CeO_2. The purpose of this study was to prepare novel photocatalysts containing ceria NPs in contact with G layers and to assess whether these semiconductors would exhibit enhanced photocatalytic activity for oxygen generation from water using Ag^+ as a sacrificial electron acceptor. Aimed at this purpose, we included in our study commercial ceria NPs and carried out the photocatalytic tests using a xenon lamp emitting UV and visible radiation. Additional tests using a UV cutoff filter (irradiation light with wavelengths higher than 380 nm) were also performed. Prior to their photocatalytic evaluation, the samples were submitted to sonication for periods longer than 1 h. This sonication has been found to be crucial to produce exfoliation of the graphenic layers leading to mono- or few-layer G. This process of exfoliation could be conveniently followed by AFM, where the number of layers in the exfoliated material can be determined. In particular, AFM images (Figure 6) show micrometric domains of G layers in agreement with the effect of the sonication to produce exfoliation of the as-synthesized G materials.

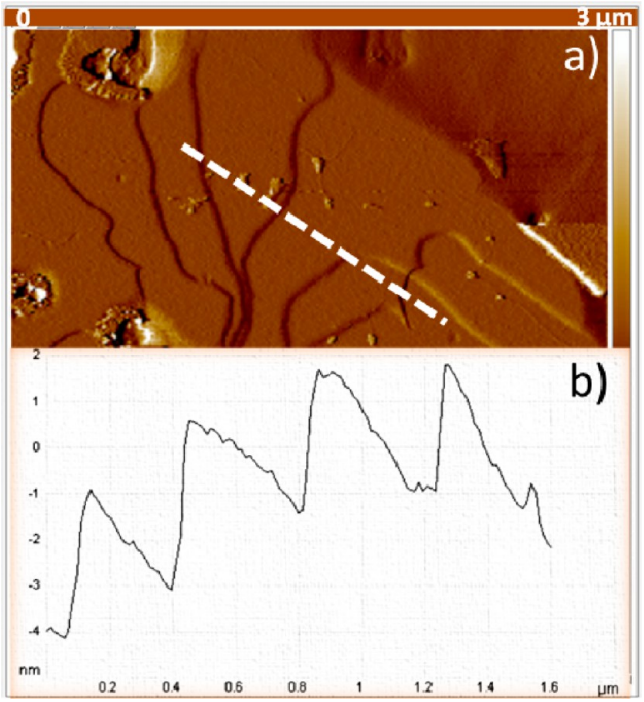

Figure 6. (a) AFM image of the $(CeO_x/G)_A$ sample taken after 1 h of sonication, in which the presence of large micrometric G sheets can be observed. (b) Vertical height measured along the lines shown in (a).

3.3. Oxygen Generation by Photocatalytic Water Oxidation. As can been seen in Figure 7, all of the ceria samples exhibited photocatalytic activity for water oxidation, but the percentage of G and the pyrolysis temperature determined the different photocatalytic activities of the resulting samples. When the G percentage was low, the photocatalytic activity of the resulting sample was comparable to that of commercial CeO_2. However, when the G percentage was higher, the photocatalytic activity of the CeO_x/G

dx.doi.org/10.1021/cs401068m | ACS Catal. 2014, 4, 497−504

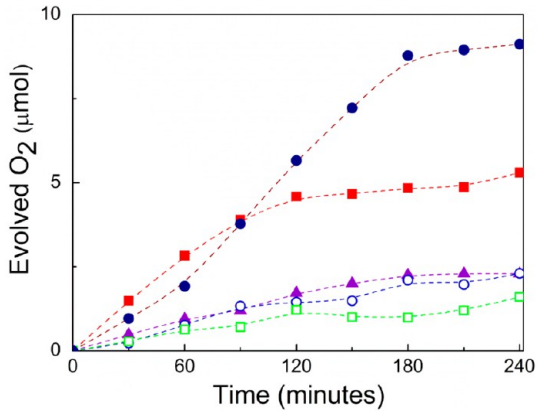

Figure 7. Oxygen evolution in photocatalytic water oxidation under UV−vis irradiation using different CeO_x/G samples as photocatalysts and CeO_2 from Aldrich as a reference: blue ●, $(CeO_2/G)_A$; red ■, $(CeO_2/G)_B$; blue ○, $(CeO_2/G)_C$; green □, $(CeO_2/G)_D$; purple ▲, CeO_2. Irradiation conditions: 0.1 M $AgNO_3$ as a sacrificial electron acceptor, 25 mL of water, 20 mg of catalyst, Xe lamp (150 W).

composite, as measured by the initial reaction rate or the total amount of oxygen evolved at the final time, was significantly higher than that of the CeO_2 control. Control experiments in which a sample of G obtained following the same experimental procedure indicated in Scheme 2 but in the absence of Ce^{3+} was used as photocatalyst did not show any photocatalytic activity for oxygen generation under the same conditions. The failure of G as well as G oxide[37,38] and other related G materials[39] to generate oxygen from water photocatalytically has been reported in the literature and has been attributed to the low oxidation potential of h^+ in these materials, which would be insufficient to oxidize water [$E°(O_2/H_2O)$ = 1.26 V]. On the other hand, the photocatalytic activity of CeO_x to generate oxygen from water has been documented in the literature.[7]

We also observed a strong influence of the pyrolysis temperature on the photocatalytic activity, with the optimal material of the series being the one in which the pyrolysis was performed at 900 °C. In the case of TiO_2, it has also been found that the optimal G percentage was in the range between 1 and 5 wt %, and also in that case the preparation conditions influenced the improvement of the photocatalytic activity.[11,12] In the present case, the most efficient composite for photocatalytic oxygen generation in the presence of Ag^+ was determined to be that in which the carbon content was 2.5 wt %. The results obtained (Figure 7) are in line with those previously found for TiO_2,[40] but in this case they refer to oxygen evolution by water oxidation, thus complementing the results reported for the photocatalytic water reduction using TiO_2 as a metal oxide semiconductor.

It was observed that the slope of oxygen generation in the time−conversion plots shown in Figure 7 decreases over the time. In the case of the most active material, $(CeO_x/G)_A$, it decreased at times longer than 3 h. Although photocatalyst deactivation could be one of the reasons for this decrease in the oxygen production rate, the most likely origin of this decrease in activity in the present case seems to be the depletion in the concentration of Ag^+ acting as the sacrificial electron acceptor as well as the increasing cloudiness and opacity of the suspension due to the formation of Ag nanoparticles.

The stability of $(CeO_x/G)_A$ under the reaction conditions is supported by the lack of observation of morphological changes of a sample submitted to prolonged irradiation (24 h) under the photocatalytic conditions. Thus, after extensive use as a photocatalyst, the $(CeO_x/G)_A$ sample was studied by TEM, whereby no apparent changes with respect to the fresh material were observed (see the Supporting Information). This characterization is compatible with the stability of the material.

Additional tests were carried out using visible light as the excitation source by cutting off the UV light with a filter (λ > 380 nm). The results shown in Figure 8 also confirm the better

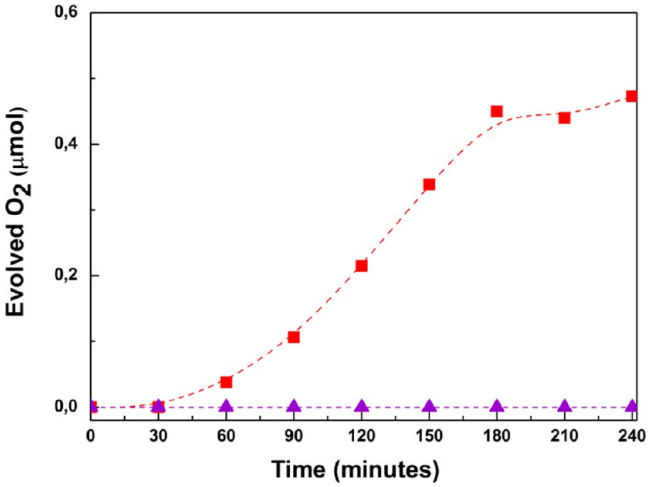

Figure 8. Oxygen evolution in photocatalytic water oxidation using Ag^+ as a sacrificial electron acceptor under visible light (λ > 380 nm) irradiation: red ■, $(CeO_x/G)_B$; purple ▲, commercial CeO_2.

performance of the CeO_x/G sample with respect to the commercial ceria control, which was unable to generate oxygen under these conditions. Comparison of the oxygen generation activities under UV−vis and visible light irradiation should take into account the fact that the relative irradiance in the visible region of the Xe lamp used was about 50% of the total irradiance as well as the preferential photoresponse of the photocatalyst. Thus, not surprisingly, a large percentage of the photocatalytic activity of CeO_x/G comes from the UV, although there is a residual visible-light phtotocatalytic activity in CeO_x/G that is absent for the commercial CeO_2 sample.

Following the rationalization accepted for TiO_2/G composites and illustrated in Scheme 1,[11,12] we speculate that a possible justification to understand the influence of G on the photocatalytic activity of CeO_x is that the contact between the two components enhances the photoinduced charge separation in CeO_x/G with respect to CeO_x. Although alternative possible explanations such as variations in the particle size and surface area or crystallinity of CeO_x cannot be ruled out, they seem less likely on the basis of the contrasting behaviors of CeO_x/G having similar particle sizes (see Table 1) and the high crystallinity observed by XRD and selected-area electron diffraction in electron microscopy.

After light absorption by the CeO_x semiconductor and promotion of electrons to the CeO_x conduction band (CB), some of these electrons would be transferred to G. Migration of the electrons from CeO_x to G would prolong the charge separation lifetime and increase the probability of the photocatalytic event. In support of this proposal, it should be recalled that the CB energy of CeO_2 NPs is very close to that of TiO_2 anatase,[41] for which this e^- migration from the semiconductor CB to G is widely accepted.[42,43] It is also worth commenting that abundant precedents in the literature

dx.doi.org/10.1021/cs401068m | ACS Catal. 2014, 4, 497−504

have shown that while G-based materials, including N- and P-doped G and G oxide, acting as photocatalysts are able to reduce water to H_2, none of these materials are able to oxidize water to oxygen.[44−46] Even a G material prepared as a control in the present study following the procedure indicated in Scheme 2 but in the absence of Ce^{4+} was unable to generate oxygen from water. Thus, it seems that the positive h^+ should not migrate to G, since otherwise these h^+ would not be able to effect H_2O oxidation.

When putting the obtained values of O_2 evolution (Figures 7 and 8) into context, one should consider that the samples did not contain a noble metal or other cocatalyst and also that oxygen generation is thermodynamically and kinetically less favorable than hydrogen formation.[47,48] Therefore, the data shown in Figures 7 and 8 indicate that our CeO_x/G composites are among the most active photocatalysts for oxygen generation from water in the presence of sacrificial electron acceptors under UV irradiation.

4. CONCLUSIONS

In the present work, we have shown that CeO_x NPs embedded on a graphitic carbon matrix can be prepared in a single step by pyrolysis of conveniently dried cerium alginate. These samples can be adequately exfoliated by sonication, and the resulting CeO_x/G suspension behaves as an enhanced photocatalyst for water oxidation using Ag^+ as a sacrificial electron acceptor. Depending on the preparation conditions, the photocatalytic activity varied considerably by around 1 order of magnitude, and the best conditions were found for the material with a G content of 2.5 wt % that was obtained by pyrolysis at 900 °C. This optimized material performed 3 times better than commercial CeO_2 NPs. Our report illustrates the advantages of using a natural biopolymer as a template in the preparation of photocatalysts. These biopolymers can not only control the particle size and the generation of a certain population of Ce^{3+} ions but also provide graphitic residue precursors of G to enhance the photocatalytic activity. The effect observed for the case of oxygen evolution using the ceria photocatalyst expands and complements the one that has been widely observed for the addition of G to TiO_2 to enhance hydrogen generation by photocatalytic water reduction.

■ ASSOCIATED CONTENT

Supporting Information

A Raman spectrum (Figure S1), XRD patterns (Figures S2 and S3), XPS spectra (Figure S4), FT-IR spectra (Figure S5), a diffuse-reflectance UV−vis spectrum (Figure S6), and TEM images (Figure S7) of various samples. This material is available free of charge via the Internet at http://pubs.acs.org.

■ AUTHOR INFORMATION

Corresponding Author

*E-mail: hgarcia@qim.upv.es.

Notes

The authors declare no competing financial interest.

■ ACKNOWLEDGMENTS

Financial support by the Spanish Ministry of Economy and Competitiviness (CTQ-2012-3532 and Severo Ochoa) is gratefully acknowledged. The Generalitat Valenciana is also thanked for financial support (Prometeo). A.P. thanks the Spanish CSIC for a research associate contract (JAE-Doc). C.L. thanks the European Commission, the European Social Fund, and the Regione Calabria for financial support of her Ph.D. fellowship and funding for her stay in Valencia.

■ REFERENCES

(1) Daghrir, R.; Drogui, P.; Robert, D. *Ind. Eng. Chem. Res.* **2013**, *52*, 3581−3599.
(2) Subramanian, V.; Wolf, E. E.; Kamat, P. V. *Langmuir* **2003**, *19*, 469−474.
(3) Xu, H.; Wang, W.; Zhu, W. *J. Phys. Chem. B* **2006**, *110*, 13829−13834.
(4) Jiang, X.; Wang, T. *Environ. Sci. Technol.* **2007**, *41*, 4441−4446.
(5) Andersson, M.; Österlund, L.; Ljungström, S.; Palmqvist, A. *J. Phys. Chem. B* **2002**, *106*, 10674−10679.
(6) Peng, T.; Zhao, D.; Dai, K.; Shi, W.; Hirao, K. *J. Phys. Chem. B* **2005**, *109*, 4947−4952.
(7) Primo, A.; Marino, T.; Corma, A.; Molinari, R.; García, H. *J. Am. Chem. Soc.* **2011**, *133*, 6930−6933.
(8) Buaki-Sogo, M.; Serra, M.; Primo, A.; Alvaro, M.; García, H. *ChemCatChem* **2013**, *5*, 513−518.
(9) Luo, Q.; Bao, L.; Wang, D.; Li, X.; An, J. *J. Phys. Chem. C* **2012**, *116*, 25806−25815.
(10) Liu, X.; Gao, Y.; Cao, C.; Luo, H.; Wang, W. *Langmuir* **2010**, *26*, 7671−7674.
(11) Zhang, Y.; Tang, Z. R.; Fu, X.; Xu, Y. J. *ACS Nano* **2010**, *4*, 7303−7314.
(12) Williams, G.; Seger, B.; Kamat, P. V. *ACS Nano* **2008**, *2*, 1487−1491.
(13) Linsebigler, A. L.; Lu, G.; Yates, J. T., Jr. *Chem. Rev.* **1995**, *95*, 735−758.
(14) An, X. Q.; Yu, J. C. *RSC Adv.* **2011**, *1*, 1426−1434.
(15) Huang, C. C.; Li, C.; Shi, G. Q. *Energy Environ. Sci.* **2012**, *5*, 8848−8868.
(16) Huang, X.; Qi, X. Y.; Boey, F.; Zhang, H. *Chem. Soc. Rev.* **2012**, *41*, 666−686.
(17) Leary, R.; Westwood, A. *Carbon* **2011**, *49*, 741−772.
(18) Xiang, Q. J.; Yu, J. G.; Jaroniec, M. *Chem. Soc. Rev.* **2012**, *41*, 782−796.
(19) Zhang, N.; Zhang, Y. H.; Xu, Y. J. *Nanoscale* **2012**, *4*, 5792−5813.
(20) Ji, Z.; Shen, X.; Li, M.; Zhou, H.; Zhu, G.; Chen, K. *Nanotechnology* **2013**, *24*, No. 115603.
(21) Srivastava, M.; Das, A. K.; Khanra, P.; Uddin, M. E.; Kim, N. H.; Lee, J. H. *J. Mater. Chem. A* **2013**, *1*, 9792−9801.
(22) Ji, Z.; Shen, X.; Yang, J.; Zhu, G.; Chen, K. *Appl. Catal., B* **2013**, *144*, 454−461.
(23) Ouwerx, C.; Velings, N.; Mestdagh, M. M.; Axelos, M. A. V. *Polym. Gels Networks* **1998**, *6*, 393−408.
(24) Wang, Z. Y.; Zhang, Q. Z.; Konno, M.; Saito, S. *Biopolymers* **1993**, *33*, 703−711.
(25) Primo, A.; Forneli, A.; Corma, A.; Garcia, H. *ChemSusChem* **2012**, *5*, 2207−2214.
(26) Primo, A.; Atienzar, P.; Sanchez, E.; Delgado, J. M.; García, H. *Chem. Commun.* **2012**, *48*, 9254−9256.
(27) Ferrari, A. C.; Basko, D. M. *Nat. Nanotechnol.* **2013**, *8*, 235−246.
(28) Ferreira, A. C.; Ferraria, A. M.; Botelho do Rego, A. M.; Gonçalves, A. P.; Girao, A. V.; Correia, R.; Gasche, T. A.; Branco, J. B. *J. Mol. Catal. A: Chem.* **2010**, *320*, 47−55.
(29) Shan, W.; Feng, Z.; Li, Z.; Zhang, J.; Shen, W.; Li, C. *J. Catal.* **2004**, *228*, 206−217.
(30) Inguanta, R.; Piazza, S.; Sunseri, C. *Nanotechnology* **2007**, *18*, No. 485605.
(31) Martínez-Arias, A.; Gamarra, D.; Fernández-García, M.; Wang, X. Q.; Hanson, J. C.; Rodriguez, J. A. *J. Catal.* **2006**, *240*, 1−7.
(32) Liu, X.; Pan, L.; Zhao, Q.; Lv, T.; Zhu, G.; Chen, T.; Lu, T.; Sun, Z.; Sun, C. *Chem. Eng. J.* **2012**, *183*, 238−243.
(33) Liu, X.; Pan, L.; Lv, T.; Sun, Z.; Sun, C. Q. *J. Colloid Interface Sci.* **2013**, *408*, 145−150.

(34) Abellán, G.; Latorre-Sánchez, M.; Fornés, V.; Ribera, A.; García, H. *Chem. Commun.* **2012**, *48*, 11416−11418.
(35) Skorodumova, N. V.; Ahuja, R.; Simak, S. I.; Abrikosov, I. A.; Johansson, B.; Lundqvist, B. I. *Phys. Rev. B* **2001**, *64*, No. 115108.
(36) Abad, A.; Concepción, P.; Corma, A.; García, H. *Angew. Chem., Int. Ed.* **2005**, *44*, 4066−4069.
(37) Latorre-Sánchez, M.; Lavorato, C.; Puche, M.; Fornés, V.; Molinari, R.; Garcia, H. *Chem.—Eur. J.* **2012**, *18*, 16774−16783.
(38) Yeh, T. F.; Chan, F. F.; Hsieh, C. T.; Teng, H. S. *J. Phys. Chem. C* **2011**, *115*, 22587−22597.
(39) Latorre-Sánchez, M.; Primo, A.; García, H. *Angew. Chem., Int. Ed.* **2013**, *52*, 11813−11816.
(40) Gomes Silva, C.; Juárez, R.; Marino, T.; Molinari, R.; García, H. *J. Am. Chem. Soc.* **2011**, *133*, 595−602.
(41) Corma, A.; Atienzar, P.; García, H.; Chane-Ching, J. *Nat. Mater.* **2004**, *3*, 394−397.
(42) Zhang, J.; Zhu, Z.; Tang, Y.; Fenq, X. *J. Mater. Chem. A* **2013**, *1*, 3752−3756.
(43) Zhang, H.; Lv, X.; Li, Y.; Wang, Y.; Li, J. *ACS Nano* **2010**, *4*, 380−386.
(44) Ng, Y. H.; Iwase, A.; Kudo, A.; Amal, R. *J. Phys. Chem. Lett.* **2010**, *1*, 2607−2612.
(45) Iwase, A.; Ng, Y. H.; Ishiguro, Y.; Kudo, A.; Amal, R. *J. Am. Chem. Soc.* **2011**, *133*, 11054−11057.
(46) Zhang, X. Y.; Li, H. P.; Cui, X. L.; Lin, Y. *J. Mater. Chem.* **2010**, *20*, 2801−2806.
(47) Grätzel, M. *Acc. Chem. Res.* **1981**, *14*, 376−384.
(48) Hoganson, W.; Babcock, G. T. *Science* **1997**, *277*, 1953−1956.